PNAS RESEARCH ARTICLE | GENETICS OPEN ACCESS

Single-cell analyses identify independent aging processes that compete to determine cellular fate in budding yeast

Manuel Hotz[a,1], Rachel G. Kroll-Ling[a,1], Nathaniel H. Thayer[a,1], and Daniel E. Gottschling[a,2]

Affiliations are included on p. 10.

Contributed by Daniel E. Gottschling; received December 1, 2025; accepted February 8, 2026; reviewed by Thomas Nyström and Jeffrey S. Smith

Phenotypic heterogeneity is prevalent during aging, yet its underlying molecular drivers remain poorly understood. In budding yeast, two distinct aging trajectories, characterized by either ribosomal DNA (rDNA) instability or mitochondrial decline, have been proposed to be mutually exclusive. Here, we systematically dissect the heterogeneity among aging yeast cells by combining single-cell transcriptomics with longitudinal fluorescence microscopy. Our data reveal distinct transcriptional responses that emerge in aging cells, highlighted by loss of rDNA silencing, a hypoxia response, and the environmental stress response (ESR). Contrary to expectation, we establish that ESR induction is not caused by rDNA instability but is instead a consequence of an early decline in mitochondrial membrane potential. However, the ESR is merely a biomarker of this decline and not itself a determinant of lifespan. While rDNA instability and mitochondrial dysfunction are anticorrelated as terminal phenotypes, we find that they are not necessarily mutually exclusive and can instead proceed concurrently within individual cells. Targeted genetic perturbations that are specific for one pathway do not impinge on the other, which is in contradiction to the idea of mutual inhibition between the two. We therefore propose a "competing hazards model", where independent aging processes progress in parallel, and the observed mode of death is determined by which process first reaches a catastrophic failure point. Our work untangles the causal links between several aging pathways and provides a framework for understanding how distinct aging trajectories emerge from independent molecular events.

yeast | phenotypic heterogeneity | single-cell RNA seq | aging | mitochondria

Significance

Phenotypic heterogeneity underlies aging, yet its molecular basis remains obscure. Using single-cell transcriptomics and longitudinal imaging in *Saccharomyces cerevisiae*, we systematically untangled independent aging pathways. We establish that the environmental stress response (ESR) is triggered by mitochondrial decline, but does not act as a lifespan determinant. Investigating the relationship between the two main declines—ribosomal DNA instability and mitochondrial dysfunction—we found that they are independent phenomena progressing concurrently, rather than being mutually inhibitory. We propose a "competing hazards" model, where aging pathways advance toward cellular death, and the observed outcome is determined by which process reaches catastrophic failure first. This framework offers an explanation of how distinct aging trajectories emerge from multiple, noninteracting molecular declines.

Organisms age with a high degree of heterogeneity, as evidenced by large phenotypic variation among individuals of a population. While genetic differences between individuals are definitely a driver of this diversity, this argument cannot be made for tissues within an organism. And yet, despite being isogenic, there are organs and cell types that are more vulnerable to the effects of aging than others (1–4). Since cells of a given tissue live and age in their individual metabolic niche within the organism, environmental differences are often invoked as drivers of phenotypic divergence (5).

However, the example of cellular aging in the budding yeast, *Saccharomyces cerevisiae,* demonstrates that even genetically identical cells living in the same environment display heterogeneity within an aging population. This organism undergoes asymmetric cell divisions and the "mother" cell produces a finite number of daughter cells that define her replicative lifespan (RLS). There is a wide distribution of RLS, ranging from very short- to long-lived individuals within the same population (6). Moreover, various cellular phenotypes manifest differently between individual aging cells (reviewed in ref. 7). Thus, to fully comprehend a process as complex and interconnected as aging, a detailed understanding of phenotypic heterogeneity is important.

Addressing heterogeneity in aging yeast, several studies have defined trajectories that individual yeast cells follow as they get older. Pioneering efforts inferred two distinct aging trajectories that result in separate terminal morphologies (Mode of Death, MoD) driven by distinct age-related phenotypes (6, 8, 9). Cells with elongated terminal morphology are characterized by promiscuous expression from the ribosomal DNA (rDNA) which occurs when rDNA genes recombine out of the repetitive array and accumulate as Extrachromosomal rDNA Circles [ERCs; (10)]. In contrast, cells with round MoD are characterized by signs of mitochondrial decline. It was proposed that these two trajectories are mutually exclusive by virtue of a mutual inhibition between some of the key players, but the underlying molecular mechanism has not been defined (9). While all this work has taken a candidate approach to define different markers of age-related decline, a comprehensive assessment of heterogeneity during aging has been limited.

[1]M.H., R.G.K.-L., and N.H.T. contributed equally to this work.

[2]To whom correspondence may be addressed. Email: dang@calicolabs.com.

This article contains supporting information online at https://www.pnas.org/lookup/suppl/doi:10.1073/pnas.2534452123/-/DCSupplemental.

Published March 11, 2026.

Several studies determined global differences between young and aged yeast cells, albeit at the population level. Transcriptionally, the most prominent changes during aging entailed the loss of silencing within the rDNA locus and the induction of the environmental stress response [ESR; (11)]. The latter is a transcriptional mechanism that leads to an upregulation of stress response genes and is accompanied by a downregulation of the translational machinery (12). In addition, increased expression of mitochondrial and metabolic genes has been observed (11). Beyond transcriptional effects, it was found that large metabolic changes occur at the bulk level during aging with cells shifting from aerobic fermentation to a more respiratory state (13). In addition, aging cells experience substantial shifts in their proteome composition and posttranslational modifications (14). However, since these studies assessed age-related phenotypes in bulk, and attempts to perform single-cell-based assays in aging yeast have been limited (15), heterogeneity among aging yeast cells has thus far not been studied systematically. In this work, we address this need by combining cross-sectional and longitudinal single-cell data to draw a more comprehensive picture of the processes involved and their interconnectivity in aging yeast cells.

Results

Single-Cell RNA-Seq (scRNA-Seq) Reveals Heterogeneity in the Aging Yeast Population. To systematically study heterogeneity among aging yeast cells, we aged wildtype (WT) cells in the Ministat Aging Device (MAD) (11) and performed scRNA-Seq at three timepoints (young, 24 h and 48 h, Fig. 1*A*) which correspond to a median replicative age of 0, 17, and 24 cell divisions, respectively (*SI Appendix,* Fig. S1*A*). These three samples were prepared for scRNA-Seq with a modified method originally described by Jackson et al. [*Materials and Methods*; (16, 17)]. We detected >1,000 cells per sample that passed our quality metrics with an average of >3,600 genes detected per cell with a minimum count of 1. We first calculated differential gene expression comparing young and aged cells and performed Gene-Set Enrichment Analysis (GSEA; Fig. 1*B*). This pseudobulk analysis revealed a strong induction of the ESR and a repression of translation-related genes in aged cells, as well as an upregulation of mitochondrial and cell wall genes (Dataset S1). In addition, we specifically examined transcripts derived from the rDNA locus (*NTS1*), which are not represented in the GSEA gene sets (see Dataset S1 for a complete list of gene sets). Here too there was a substantial upregulation in expression during aging (Fig. 1 *C*, *Left* plot). Overall, at the population level our single-cell data showed gene expression changes reminiscent of published bulk RNA-Seq data (11).

We then analyzed our data at the single-cell level. Cells of the "young cell" sample, which is an exponentially growing cell culture, displayed a Uniform Manifold Approximation and Projection (UMAP) structure largely driven by the cell cycle (*SI Appendix,* Fig. S2*A*), as described previously (16). Among aged cells, however, it became apparent that there was a large degree of heterogeneity in gene expression between individual cells that was beyond the cell cycle signatures (Fig. 1*C*). Specifically, rDNA-derived transcripts and ESR genes increased in expression in older cells, but to a variable extent within the population. Likewise, the expression of ribosomal (RP) genes were reduced nonuniformly between cells with age. This variability in gene expression was apparent when plotting 48 h aged cells separately in UMAPs (Fig. 1*D*), or all ages combined (*SI Appendix,* Fig. S2*B*). The ESR formed a gradient across the UMAP from cells with almost no ESR expression to cells with very high levels, while expression of the RP genes showed the opposite pattern (Fig. 1*D*). This is in agreement with earlier conclusions that cells with high ESR levels are generally low in translation-related gene expression (12, 18). Levels of rDNA-derived transcripts were variable as well, but their expression pattern appeared uncorrelated with that of ESR and RP genes. The fact that these major gene signatures showed differential relationships between one another led us to examine the gene expression patterns more systematically.

Distinct Transcriptional Responses Emerge in Aged Cells. In order to ask which different independent transcriptional responses appeared in aged yeast cells, we performed a coexpression analysis using gene-by-gene correlations for the 48 h timepoint. In short, a Spearman correlation coefficient was calculated for every gene pair, and all genes having two or more meaningful correlations with any other gene (Spearman coefficient > 0.5) were clustered into a heatmap (Fig. 2*A* and *SI Appendix,* Fig. S3*A*). This analysis revealed several gene clusters with varying relationships to each other. The two biggest groups with a very strong internal correlation were the ESR genes and ribosome biogenesis genes (257 and 316 genes, respectively), which were also very strongly anticorrelated with each other (Fig. 2 *A* and *B*, *Top* plot). Interestingly, while a majority of genes in the ESR cluster were bona fide stress-induced ESR genes (12) and known Msn2 or Hsf1 targets (Dataset S3), there were also subclusters of respiration-related mitochondrial genes (*ATP*, *COX*, *QCR* genes) that correlated well with the rest of the ESR genes. This suggests that there was a connection between ESR induction and mitochondria during aging. Apart from these two large gene groups (ESR and RP), there were smaller gene clusters, such as one containing transcripts from the rDNA locus (*NTS1* and other transcripts encoded in the rDNA repeat), and several cell cycle gene clusters (Fig. 2*A*). There was also a group of genes characterized by being induced upon oxygen or heme starvation (from now on referred to as "Hypoxia genes"; Dataset S3). Specifically, this latter cluster contained a number of targets of the transcription factor Rox1, a heme-dependent regulator of hypoxic genes (*ANB1*, *DAN1*, *HEM13* etc), and targets of the transcription factor Bas1 (*ADE* genes), which is induced in anaerobic conditions (19). Included in this cluster were also a number of glycolytic genes, consistent with the notion that glycolysis is tied to oxygen and heme availability ["Pasteur effect", (20)]. In agreement with the idea that the three subclusters of hypoxia genes are expressed in response to the same trigger, the expression patterns across individual cells were comparable between the subclusters (*SI Appendix,* Fig. S3*B*).

Interestingly, despite the fact that loss of rDNA silencing and accumulation of ERCs are well characterized aging factors (10), no significant correlation between rDNA transcripts and the dominant ESR signature was observed (Fig. 2 *B*, *Middle* plot). This suggests that despite the impact of ERC accumulation on lifespan, it is not responsible for the induction of this stress response. In contrast, there was a weak but significant anticorrelation between rDNA and Hypoxia genes, reminiscent of a previously suggested mutual exclusion between mitochondrial decline and loss of rDNA silencing [Fig. 2 *B*, *Bottom* plot, (9)]. Together, we detect at least three heterogeneous transcriptional programs among aging cells: ESR induction and concomitant RP gene repression, loss of rDNA silencing and a hypoxia-related response.

Longitudinal Imaging Reveals Distinct Transcriptional Signatures during Aging. While the scRNA-Seq data provide detailed single-cell level transcriptional information at each timepoint sampled along the aging process, it lacks longitudinal information (a cell's history, final lifespan, and terminal morphology), which define

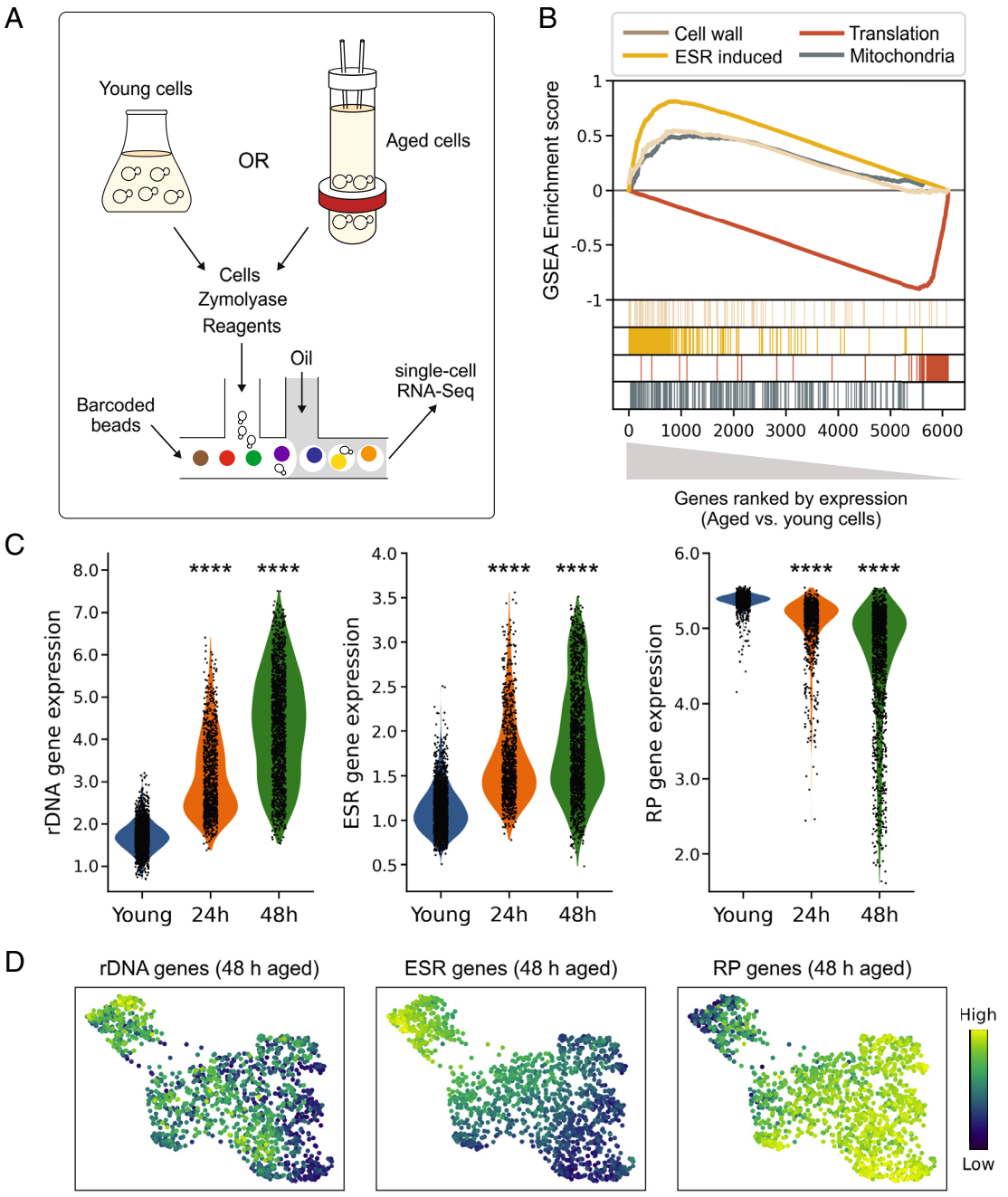

Fig. 1. scRNA-Seq on aged yeast cells reveals heterogeneity in the population. (*A*): Schematic of the workflow for cell aging and scRNA-Seq. (*B*): GSEA on the differential gene expression comparing young and 48 h aged cells (t-score). Selected gene ontology terms are shown. (*C*): Mean expression of rDNA transcripts (*Left*), ESR genes [as defined by Gasch et al. (12), *Center*] and RP genes (*Right*) in young or aged cells. Values are log-transformed (counts per million). Asterisks are from Wilcoxon Rank-Sum test (*P*-value < 10^{12}). n = 1,500 cells. (*D*) UMAPs with mean expression of gene groups corresponding to C in aged cells (48 h). n = 1,500 cells.

the RLS aging process and establish causality between a mother cell's lifespan-determining events. In order to collect this type of information, we constructed fluorescent markers representing the three major transcriptional responses described above, and used a microfluidic tool combined with automated image analysis [Yeast Lifespan Machine, YLM, (21)]. The YLM enables us to track reporter gene expression throughout the entire lifespan of hundreds of individual cells and reveals the relationship between Replicative and Temporal Lifespan (number of divisions vs. time a cell is alive; *SI Appendix*, Fig. S1 *B* and *C*) for every cell. To visualize loss of rDNA silencing and ERC accumulation we tagged the nucleolar protein Srp40, as nucleolar enlargement was previously found to be indicative of ERC accumulation (10). We validated this reporter by aging cells expressing Srp40-mNeon for 48 h in the MADs and then used Fluorescence-Activated Cell Sorting to separate the aged cells into high and low Srp40-mNeon subpopulations (top and bottom 25%). ScRNA-Seq on these subpopulations showed that the rDNA-derived transcript *NTS1-2* was the most differentially expressed transcript between "High Srp40" and "Low Srp40" cells (*SI Appendix*, Fig. S4 and Dataset S1), which confirms the utility and accuracy of Srp40-mNeon as a marker for loss of rDNA silencing and ERC accumulation. As a marker for Hypoxia gene induction, we used a transcriptional *HEM13* reporter (pHEM13-mNeon), since *HEM13* was significantly correlated with other

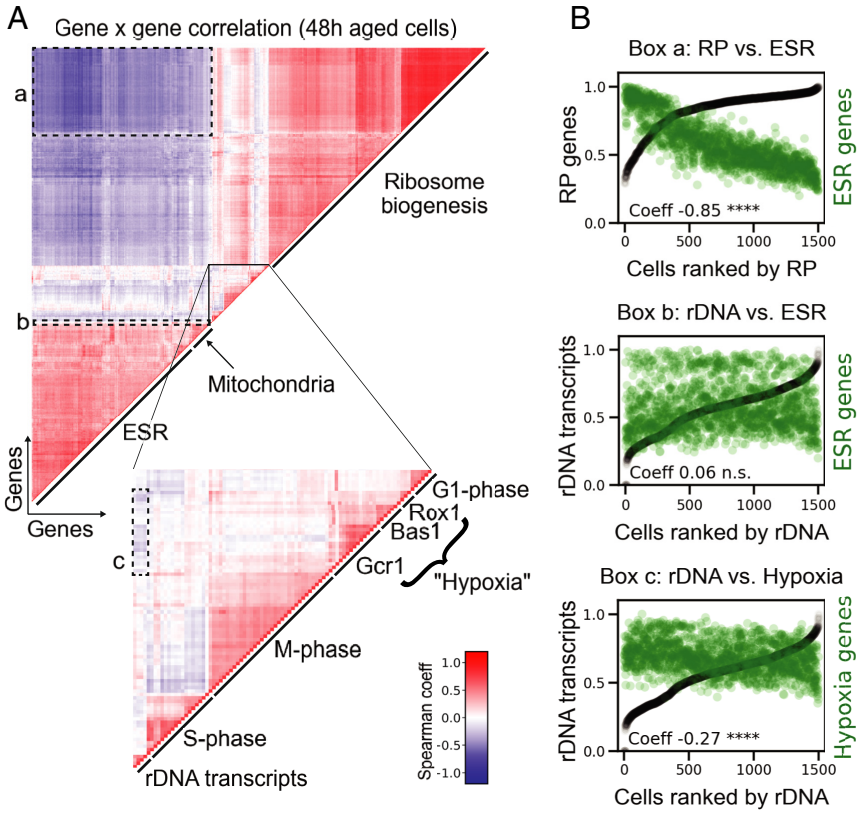

Fig. 2. Several distinct transcriptional responses emerge in aged cells. (*A*) Clustered gene-by-gene correlation matrix using the scRNA-Seq expression data from aged cells (48 h). For every gene pair the Spearman correlation was calculated across individual cells and assembled by hierarchical clustering. Dotted lines highlight groups of genes that are plotted in *B*. Only genes with >2 correlations with a Spearman coefficient >0.5 were included in the matrix (n = 664 genes). (*B*) Examples of correlations for various groups of genes. *Top*: RP vs. ESR gene expression (Box *a*). *Center*: rDNA transcripts vs. ESR gene expression (Box *b*). *Bottom*: rDNA transcripts vs. Hypoxia gene expression (Box *c*). Asterisks represent *P*-value < 10^{-27}.

genes within this cluster (*SI Appendix,* Fig. S3*C*). Finally, we tagged the bona fide ESR target Hsp12 (12, 22) to monitor ESR induction longitudinally in the YLM.

The longitudinal imaging data revealed several distinct patterns. The rDNA/ERC related signal (Srp40-mNeon) increased dramatically toward the end of life, in particular in cells dying with elongated MoD, whereas the *HEM13* signal was stronger in cells with round MoD (Fig. 3 *A* and *B*). However, while these two signals were anticorrelated late in life when comparing elongated and round cells, they were not necessarily anticorrelated throughout life. Specifically, high Srp40 fluorescence appeared to be a terminal phenotype of elongated cells, whereas the *HEM13* signal was more variable between and throughout lifespans, though generally higher in round MoD cells. In contrast to both Srp40 and *HEM13*, the ESR marker Hsp12-mNeon was indistinguishable between cells of elongated and round MoD with a general tendency to increase with age. Thus, as suggested by the scRNA-Seq data, the induction of the ESR seems unlinked to ERC accumulation. Overall, the results from longitudinal imaging supported the idea derived from transcriptional data that there were distinct and heterogeneous transcriptional responses in aged cells.

Mitochondrial Decline Leads to ESR Induction in Early Aging. As mentioned above, the induction of the ESR was not the result of loss of rDNA silencing and ERC accumulation, raising the question of what triggered the ESR during aging. It has previously been demonstrated that mitochondrial function and, in particular, the mitochondrial membrane potential (MMP) declines during aging in yeast (23, 24). Remarkably, MMP begins to deteriorate early in life particularly in shorter-lived cells, i.e., with kinetics that could suggest a link to the observed ESR induction (Fig. 3). Moreover, a subset of mitochondrial genes coclustered with the ESR in the scRNA-Seq data (Fig. 2*A*), suggesting a connection between the two phenomena. To address this directly, we performed longitudinal imaging in the YLM on cells coexpressing the MMP-dependent reporter [preCOX4-mNeon-SL17, (24)] together with the ESR reporter Hsp12-mCherry (Fig. 4 *A* and *F*). Here we found that early MMP decline coincided with an increase in ESR expression, with lower MMP generally associated with higher ESR expression, an anticorrelation that is also apparent when sorting cells by their MMP signal at 24 h (*SI Appendix,* Fig. S5*A*). Together, these results suggest that mitochondrial decline and ESR induction are indeed connected during aging, consistent with previous reports (25).

In order to better understand the relationship between MMP and ESR, we examined transcriptional signatures between aged cells with high and low MMP expressing the dual component version of the recently described MMP reporter [preCOX4-mNeon-SL17 and Tim50-mCherry, (24)]. 24 h aged cells were separated into "high MMP" and "low MMP" (top and bottom 25% of MMP ratio) by FACS. scRNA-Seq was then performed on the subpopulations, allowing us to tie transcriptional changes to this non-transcriptional reporter (Fig. 4*B*). The scRNA-Seq revealed two striking differences between cells with high or low MMP. First, there was an induction of mitochondrial gene expression when MMP was low (gene ontology term "mitochondrial inner membrane," Fig. 4*D* and *SI Appendix,* Fig. S4*B*), suggesting that cells with declining mitochondrial function increased mitochondrial

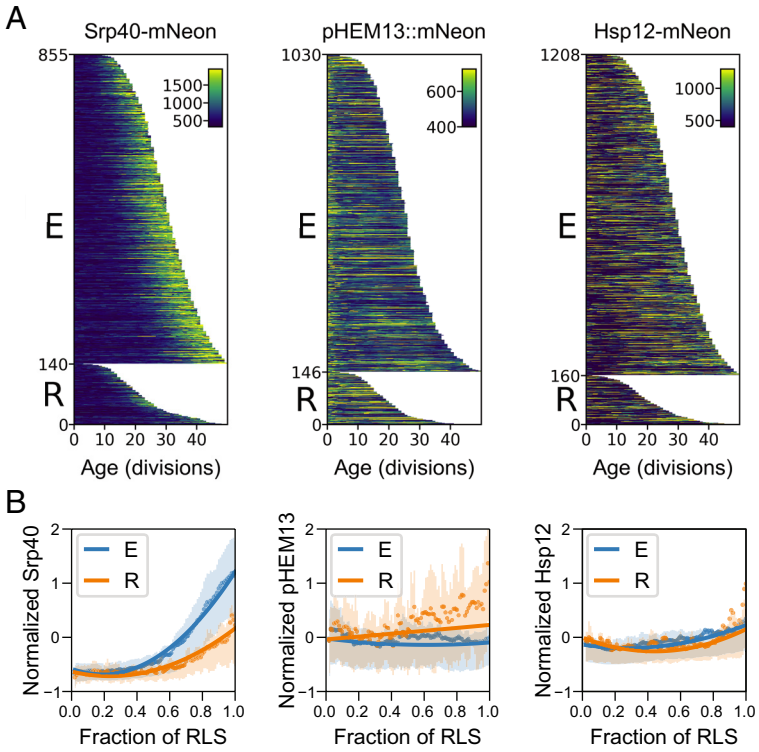

Fig. 3. Distinct transcriptional signatures revealed by longitudinal imaging of fluorescent reporters. (*A*) Heatmaps of longitudinal imaging data from cell birth to death. Srp40-mNeon reports on nucleolar enlargement and ERC accumulation, pHEM13-mNeon on the hypoxia response and Hsp12-mNeon on ESR gene expression. Cells are grouped by elongated (E) and round (R) MoD and sorted by RLS. (*B*) Quantification of data in A, z-score normalized per fluorescent reporter. Circles are smoothened mean values, shaded regions are the inner quartiles and solid lines are fits from Linear Mixed-Effects Models (*Materials and Methods*).

gene expression, perhaps in an attempt to compensate for MMP loss. Second, the ESR was strongly upregulated in low MMP cells, further supporting the notion that MMP decline and ESR induction are functionally linked in aging cells (Fig. 4*C* and *SI Appendix,* Fig. S5*B*).

To address whether there was a causal link between the ESR and MMP, the ESR master regulator *MSN2* was deleted and cells were longitudinally examined with the ESR and MMP reporters. As expected, *msn2Δ* cells had virtually no detectable Hsp12 fluorescence (Fig. 4 *E* and *G*), along with reduced expression of a majority of ESR genes (*SI Appendix,* Fig. S6 *A* and *B*). However, while efficiently abrogating the ESR, deleting *MSN2* had no effect on the kinetics of MMP decline, suggesting that ESR induction does not lead to mitochondrial decline. Conversely, when the gene *SIS2* was deleted, which enhances MMP and rescues its decline during aging (24), the ESR was significantly suppressed (Fig. 4 *F* and *G*). This also occurred with a deletion of *HDA2*, a second and independent intervention that suppresses MMP decline [*SI Appendix,* Fig. S7 *A* and *B*, (24)]. As an orthogonal method to analyze these data we applied Cox-Proportional Hazard modeling (*Materials and Methods*). This analysis showed that deletion of *SIS2* and *HDA2* both reduced the hazard of ESR induction at any given age, i.e., delayed it, whereas deletion of *MSN2* did not affect the hazard of losing MMP. Together, these analyses demonstrate that the ESR is induced by mitochondrial dysfunction during aging, specifically by the reduction of MMP.

Given that improved maintenance of MMP through life correlates with increased lifespan (24), we tested whether ESR induction had any effect on the longevity of cells. Despite the magnitude of this stress response during aging and consistent with previous findings (26), the lifespan of *msn2Δ* knockout cells was virtually identical to that of WT cells (Fig. 4*H*). We excluded a compensatory effect of the *MSN2* paralogue *MSN4*, because the *msn2Δ msn4Δ* double knockout affected ESR genes similarly (*SI Appendix,* Fig. S6 *A* and *B*), and yet lifespan remained unaffected compared to WT (Fig. 4*H*). We note that strains with comparable rDNA copy number (CN) were used in all lifespan comparisons (Dataset S4), in order to eliminate contributions of rDNA CN to RLS (27). Together, these data suggest that while MMP decline itself is tied to cellular lifespan and efficiently triggers the ESR, the induction of this stress response itself has no beneficial effect on longevity under the conditions tested here.

A question that remained was how the two mitochondria-related phenomena—MMP decline and the induction of a hypoxia response—were related to each other in our data. MMP is a well-established readout for mitochondrial health, and oxygen and heme are required for mitochondrial function as well. However, in the scRNA-Seq experiment on the entire aging population (Figs. 1 and 2) there was no significant correlation between MMP decline (as inferred by ESR induction) and the hypoxia response. To directly test for a potential connection, we coexpressed the MMP reporter preCOX4-mNeon and cytoplasmic iRFP and imaged these cells longitudinally in the YLM. The fluorophore iRFP-713 directly reports on cellular heme levels, since it requires the heme-related molecule biliverdin to fluoresce (9, 28) (*SI Appendix,* Fig. S8*A*). Cytoplasmically expressed iRFP responded accurately to varying heme levels and was substantially anticorrelated with the fluorescence pattern of the hypoxia reporter pHEM13-mNeon throughout the lifespan of yeast cells (*SI Appendix,* Fig. S8 *B–D*). The iRFP reporter showed an overall similar pattern compared with MMP, with both signals decreasing in many cells early during aging, while staying high throughout life or increasing late in other cells (*SI Appendix,* Fig. S9*A*). The correlation between the two reporters became more obvious when sorting cells by their MMP signal at 24 h (*SI Appendix,* Fig. S9*B*).

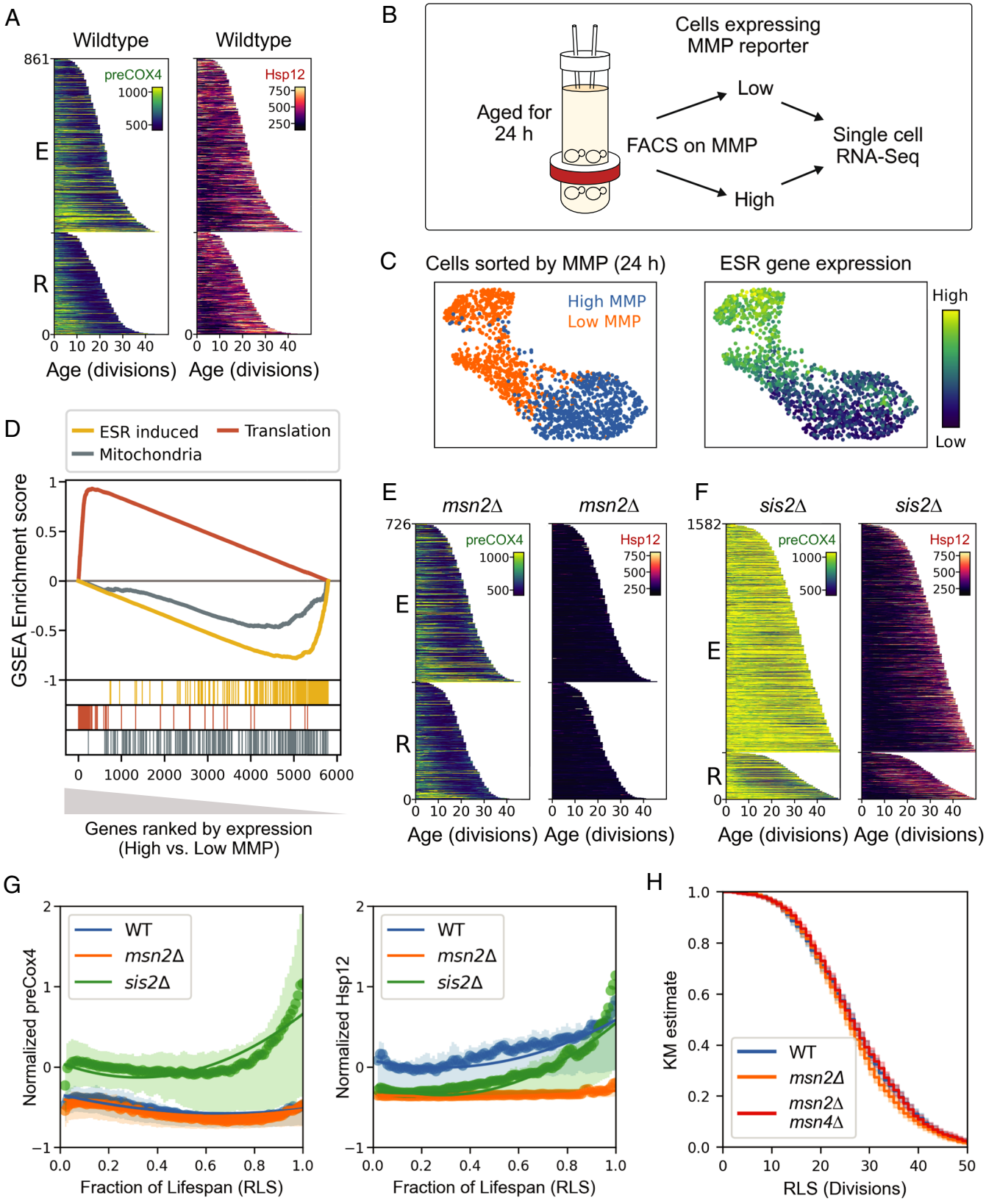

Fig. 4. Loss of MMP triggers ESR induction. (*A*) Heatmaps of longitudinal imaging data from cell birth to death. preCOX4-mNeon reports on MMP, Hsp12-mCherry on ESR gene expression. Cells are grouped by elongated (E) and round (R) MoD and sorted by RLS. (*B*) Schematic of the workflow for cell aging and scRNA-Seq combined with FACS of the MMP reporter. (*C*) Combined UMAPs of the *Top* ("High MMP") and *Bottom* ("Low MMP") 25% of cells after sorting by MMP. Sample distribution in UMAP (*Left*) and mean ESR gene expression (*Right*) is shown. n = 750 cells per sample. (*D*) GSEA on the differential gene expression comparing "High MMP" and "Low MMP" cells (t-score). Selected gene ontology terms are shown. (*E* and *F*) Heatmaps of longitudinal imaging data from cell birth to death for *msn2Δ* cells (*E*) and *sis2Δ* cells (*F*) using preCOX4-mNeon and Hsp12-mCherry as reporters. (*G*) Quantification of data in *A*, *E*, and *F*, z-score normalized per fluorescent reporter. Circles are smoothened mean values, shaded regions are the inner quartiles and solid lines are fits from Linear Mixed-Effects Models (*Materials and Methods*). (*H*) Kaplan–Meier estimates of the survival function for WT, *msn2Δ*, and *msn2Δ msn4Δ* cells.

However, this analysis also showed that the signals were not strictly correlated, since for example the cells with the brightest MMP signal were not the highest in iRFP as well. In conclusion, it appears that MMP reporter decline and hypoxia gene induction occur in an overlapping subpopulation and with similar kinetics, but the correlation was not strong enough to be apparent in a cross-sectional dataset such as the scRNA-Seq time course. This likely indicates that the MMP reduction and hypoxia gene induction are both reflecting aspects of mitochondrial decline, but only MMP reporter decline is tightly linked to ESR induction.

Competing Hazards of Independent Processes, Rather than Mutual Inhibition Results in Two Modes of Death. As mentioned above, there was a significant, but weak anticorrelation between ERC accumulation and hypoxia gene induction (Fig. 2 *A* and *B*). This observation has been made before and led to a model where mutual inhibition between the rDNA-related decline and loss of mitochondrial function results in two distinct trajectories and ultimately explains the existence of two MoDs (9). Importantly, this model requires a strong mutual exclusion between the two phenomena and predicts that cells will rarely show signs of both in decline. In order to test this prediction directly, cells coexpressing Srp40-mCherry and the heme reporter iRFP were imaged longitudinally in the YLM (Fig. 5*A*). As before, Srp40 levels strongly increased at the end of life in cells undergoing elongated MoD, while being substantially lower in cells with round MoD. In contrast, there was not a strong difference in iRFP signal between elongated and round MoD cells throughout lifespan. This became particularly obvious when plotting the mean terminal fluorescence (five frames before death), which was clearly distinct between elongated and round MoD cells for Srp40, while iRFP only showed little difference (Fig. 5*B*). Likewise, when cells were grouped by their terminal iRFP signal, which highlights the existence of "High iRFP" and "Low iRFP" cells, Srp40 was not strictly separated between the two subgroups of cells, by either longitudinal or terminal fluorescence (*SI Appendix,* Fig. S10 *A* and *B*). Thus, there is no strict mutual exclusion between iRFP decline and Srp40 accumulation among aging cells.

To test the idea of mutual inhibition between ERCs and mitochondrial decline, we used genetic interventions to perturb these two phenomena. As done before (9), we first deleted *SIR2*, an NAD-dependent histone deacetylase of the Sirtuin family, which, among other functions, acts as a suppressor of ERC formation (29–31). Consistent with published data, *sir2Δ* cells not only had increased ERCs levels (Srp40-mCherry), but showed higher cellular heme levels as well (iRFP; Fig. 5 *C*, *F*, and *G*). This effect could in fact suggest that worsening ERC accumulation prevents mitochondrial decline and would therefore be consistent with the idea of mutual inhibition. However, it is important to consider that Sir2 has a plethora of targets in its role as histone deacetylase, and deleting the gene has pleiotropic effects (29–31). Furthermore, several studies intimately link Sir2 to mitochondrial function, invoking the fact that Sir2 utilizes NAD+ as a cofactor (32, 33), and to mitochondrial quality control (34). Thus, deleting *SIR2* likely connects both ERCs and mitochondrial decline by acting upstream of both phenotypes, and is therefore unsuitable for uncoupling the two phenotypes.

As a more targeted intervention, we first reduced rDNA-related phenotypes by deleting *FOB1*, a well-known intervention that prolongs lifespan by reducing ERC formation and has no other known consequences to the cell (11, 35). As expected, this mutation led to a strong delay in onset and reduction in Srp40 signal with age, a reduction in elongated MoD and longer lifespan. In contrast, deletion of *FOB1* did not significantly affect iRFP levels, as determined by Linear Mixed-Effects modeling, suggesting that ERC accumulation had no effect on the progression of mitochondrial decline (Fig. 5 *D*, *F*, and *G*). Conversely, deleting *SIS2* resulted in the expected increase in heme levels in concordance with its role in maintaining mitochondrial function during aging (24), but did not lead to an increase in Srp40 signal (Fig. 5 *E*–*G*). These data suggest that there is no mutual inhibition between ERC accumulation and mitochondrial decline, and this was reinforced with Cox-Proportional Hazard modeling (*SI Appendix,* Fig. S10 *C* and *D*; *Materials and Methods*). Deletion of *FOB1* reduced the hazard of ERC accumulation at any given age, while it had no effect on the hazard of heme loss. Conversely, deleting *SIS2* did not exacerbate the risk of ERC accumulation. Taken together, these analyses show that ERC accumulation and mitochondria-related decline can occur independently of one another without any detectable inhibition between these two aging processes.

In summary, our data suggest that the existence of two modes-of-death are likely the result of independent competing hazards, rather than a direct interaction between the two underlying phenomena. Both rDNA-related decline and mitochondrial dysfunction lead to distinct terminal phenotypes, with the former leading to a dramatic increase in ERCs shortly before cell death, while the latter results in irreversible mitochondrial decline ultimately leading to complete loss of respiratory function [*SI Appendix,* Fig. S11, (36)]. It is therefore conceivable that whichever of the two dysfunctions happens first and progresses more rapidly will simply overshadow the effects of the other, or kill the cell before those effects would become apparent. This mutual exclusion of terminal phenotypes is reflected in distinct MoDs and creates the appearance of mutually exclusive trajectories.

Discussion

A fundamental challenge in aging biology is to understand the phenotypic heterogeneity among aging individuals. Budding yeast provides an ideal system to dissect this problem at its core, since genetics and environment are readily controllable in this organism. By developing and applying single-cell transcriptomic techniques to aging yeast, we have systematically mapped this heterogeneity. Our analysis reveals what bulk population studies could not: that seemingly correlated pathways of aging can be entirely uncoupled in individual cells and conversely, that previously unconnected mechanisms are in fact causally linked. This high-resolution view allowed us to move toward untangling the complex interplay of age-related declines and led us to propose a model for how distinct aging trajectories emerge.

As one conclusion, we found that the ESR is a marker of mitochondrial decline, rather than a driver of aging. Our single-cell approach resolved a long-standing ambiguity from bulk-level studies: while both rDNA instability and the ESR are known aging phenotypes, we found they are completely uncorrelated at the single-cell level. Instead, we established a causal relationship between the age-related decline in MMP and the ESR. However, this stress response appears to be a phenotypic dead-end with respect to longevity: while mitochondrial health itself is a critical determinant of lifespan (23, 24), the downstream stress response is not. Genetically abrogating the ESR had no effect on lifespan, suggesting it is a passive biomarker of mitochondrial damage, not an active modulator of aging itself. This is a crucial distinction that could only be made by causally linking disparate phenotypes within single cells over time.

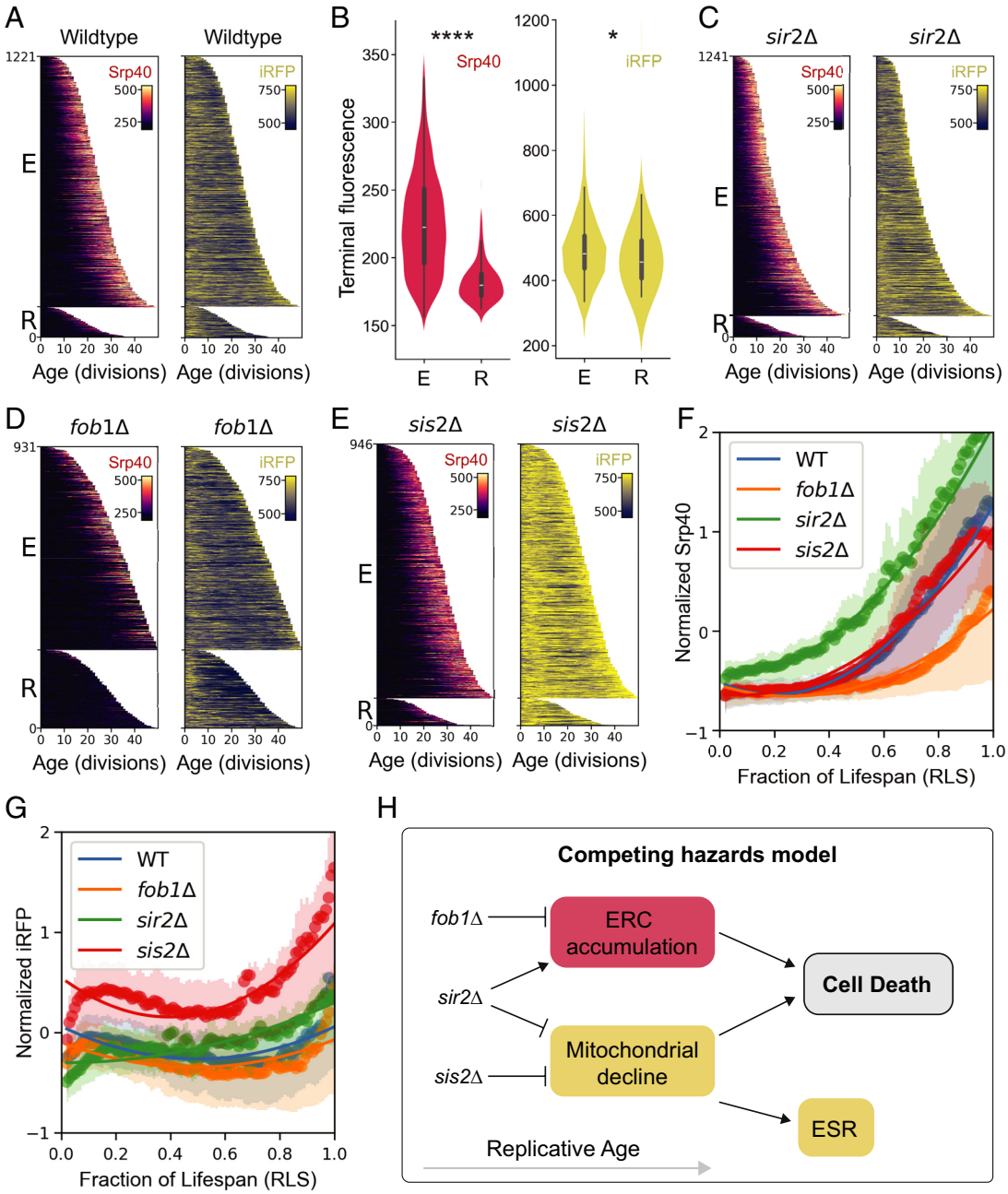

Fig. 5. Competing hazards rather than mutual inhibition between ERCs and mitochondrial decline lead to distinct cellular fates. (*A*) Heatmaps of longitudinal imaging data from cell birth to death in WT cells. Srp40-mCherry reports on nucleolar enlargement and ERC accumulation, cytoplasmic iRFP on cellular heme levels. Cells are grouped by elongated (E) and round (R) MoD and sorted by RLS. (*B*) Quantification of data in *A*. Mean terminal fluorescence (five frames before death) is plotted for both reporters. Asterisks are from Wilcoxon Rank-Sum test (**** for *P*-value < 10^{-40}, * for *P*-value < 10^{-3}). (*C–E*) Heatmaps of longitudinal imaging data from cell birth to death in *sir2Δ* (*C*), *fob1Δ* (*D*), and *sis2Δ* (*E*) cells. (*F* and *G*) Quantifications of *A*, *C–E*, z-score normalized per fluorescent reporter. Circles are smoothened mean values, shaded regions are the inner quartiles and solid lines are fits from Linear Mixed-Effects Models (*Materials and Methods*). (*H*) Competing hazards model for aging. rDNA and mitochondria-related decline are independently acting phenomena that competitively affect lifespan.

Why might the ESR be invoked by mitochondrial dysfunction? A direct consequence of MMP decline is a reduction in protein import capacity into the mitochondria and it was previously shown that multiple stress responses are triggered when mitochondrial protein import is impaired (reviewed in ref. 37). Although not strictly limited to classical ESR targets, these stress responses share many characteristics of the ESR: increased expression of chaperones and reduced expression of translation-related genes. It is therefore conceivable that MMP decline directly triggers the ESR through its effect on mitochondrial protein import.

Our findings also provide a contrasting view of the "mutual inhibition" model, which was proposed to explain the two distinct modes of death observed in yeast (9). Our data confirm the anti-correlation between rDNA instability and mitochondrial decline as terminal phenotypes and also invoke Sir2 as an upstream regulator of both ERC formation and mitochondrial function. However, when perturbing with greater precision only one of these aging phenotypes, our experiments contradict the existence of an underlying inhibitory switch between two trajectories. We found a substantial number of cells in which both trajectories proceeded concurrently. More definitively, our genetic perturbations showed

no evidence of cross-pathway inhibition. Suppressing ERC formation by deleting *FOB1* did not worsen mitochondrial decline, and improving mitochondrial health by deleting *SIS2* did not accelerate ERC accumulation. Therefore, while the two pathways are indeed anticorrelated within the aging cell population, there is no evidence for mutual inhibition between them.

This study also highlights how the specificity of a perturbation to test causal links in aging can lead to different conclusions. Deletion of *FOB1*, which is quite specific for action at the rDNA locus and ERC formation, provides great precision for perturbing the ERC pathway and permits an uncomplicated interpretation of changes in the mitochondrial pathway of aging. By contrast, perturbation of *SIR2* is much more pleiotropic on the cell: its activity is tied to mitochondrial function and quality control and affects multiple aspects of cell physiology (38), in addition to its impact on the rDNA locus and ERC formation. This reinforces the importance of knowing the mechanisms of action by which a perturbation works, in order to develop a clearer understanding of the cellular aging process.

If not by mutual inhibition, how can two distinct modes of death arise? We propose a "competing hazards" model that offers a solution to this paradox. In this framework, rDNA instability and mitochondrial decline are two independent and parallel processes of cellular deterioration. They are not directly interacting, but progress toward a catastrophic, irreversible failure point within a cell. The observed MoD reflects which process reaches its respective failure point first. A cell that first succumbs to catastrophic ERC accumulation dies with an elongated morphology, terminating that lineage before mitochondrial failure can become the terminal event. Conversely, a cell whose mitochondrial function collapses dies with a round morphology before ERC accumulation becomes the catastrophic event. This competition creates the appearance of mutually exclusive outcomes from endpoint data, when in fact the underlying processes are independent.

What lessons that extend into mammalian aging biology can be learned from our study? Metazoa exist as multicellular systems with distinct organs, tissues, and cell types that are readily distinguishable transcriptionally and functionally. However, it remains unclear whether, as an organism ages, there is heterogeneity among cells within one cell type. The example of yeast demonstrates that, even among cells of one type living in an identical and constant environment, aging can result in different phenotypic outcomes as a result of complex interactions—or lack thereof—between aging phenotypes. These conclusions were only possible by studying aging at the single-cell level both cross-sectionally and longitudinally. We therefore expect that extending this type of approach to higher eukaryotes in order to resolve intracell type heterogeneity during aging will likely lead to a better understanding of aging biology.

Materials and Methods

Yeast Strains and Media. All strains are in the S288C background (Dataset S4) and derived from a WT strain with a corrected PTR3 allele (24). Strains carrying gene deletions were constructed by transformation using plasmids and oligos as described in ref. 39. Strains expressing fluorescent reporters were constructed as follows. Endogenous C-terminal tagged strains were made by transformation using integration cassettes amplified from pKT127-derived plasmids (40). The pKT127-mNeonGreen-NatMX vector was made by replacing the KanMX cassette with NatMX using the restriction sites BglII and SpeI. The *HEM13* expression reporter was constructed by NEB HiFi DNA Assembly. 500 bases upstream of the *HEM13* start codon were added in frame with mNeonGreen on a pKT127 vector. The construct was PCR amplified and integrated into an empty region of Chromosome I (199447. 199460). The iRFP construct was made by NEB HiFi DNA Assembly using a yeast codon optimized gBlock of iRFP713 [(28); Integrated DNA Technologies] that was cloned into pHO-KanMX (41) containing a *TEF1* promoter and a *CYC1* terminator, as well as homology to the endogenous HO locus. The iRFP reporter strain was generated by NotI digestion and transformation into the HO locus.

Unless otherwise specified, all experiments utilized synthetic complete (SC) medium. The SC medium comprised SC mix, yeast nitrogen base (YNB) with ammonium sulfate (Sunrise Science), and 2% glucose at pH 4.5. For aging experiments using the MAD system (11), three alterations were implemented: regular YNB was substituted with biotin-free YNB (Sunrise Science), 40 nM 7,8-diaminopelargonic acid was added to compensate for the absence of biotin, and 2% methyl-alpha-D-mannopyranoside (Sigma-Aldrich) was added to prevent cell aggregation during the experiment (27).

MADs. For experiments using the MAD system a previously described protocol was used (11, 27). In brief, cells were pregrown in biotin-free medium for 24 h at an Optical Density < 0.05 and five ODs were harvested per MAD. Cells were washed three times with PBS and then incubated with 0.5 mg Sulfo-NHS-LC-LC-Biotin (Sigma-Aldrich) per OD for 30 min at room temperature. Biotinylated cells were then washed extensively with medium and grown in flasks at 30 °C for 4 to 5 h. Cells were then incubated with 20 μL of Dynabeads MyOne Streptavidin C1 magnetic beads (Thermo Fisher) in medium and incubated for 10 min at room temperature. Cells were harvested on a 0.22-μm filter (Corning) and bead-labeled mother cells were extracted from the culture by repeated washing on a DynaMag-2 magnet (Invitrogen). Finally, cells were loaded into a MAD prefilled with medium and let bind to the magnet for 5 min before the media pumps were turned on. Cells were either harvested after 24 or 48 h as indicated. For the latter, MADs were washed after 24 h to avoid overcrowding by briefly taking the vessel off the magnet with the media pump paused and then allowing the cells to rebind to the magnet for 5 min before pumps were turned back on.

scRNA-Seq and Analysis. ScRNA-Seq experiments were performed on either young (exponentially growing) cells or cells aged in MADs that had been purified on magnets as described above. After harvesting, cells were washed in Tris Azide Fluoride buffer (1 M Sorbitol, 100 mM Tris base, 20 mM sodium azide, 20 mM sodium fluoride, 0.1 mg/μL BSA at pH 8.5) with 1 U/μL Protector RNase Inhibitor (Sigma-Aldrich) and adjusted to a concentration of 500 cells/μL. The TAF buffer ensures that mRNA is stable, while retaining functional proteins in the cell to allow for fluorophore-based assays such as FACS. Then, scRNA-Seq was performed using the Chromium GEM-X Single Cell 3′ Kit v4 or the Chromium Next GEM Single Cell 3′ LT kit v3.1 (10× Genomics) with two modifications: five Units of Zymolyase (Zymo Research) were added to the RT Master Mix immediately before cells were loaded into the Chromium GEM-X chip and an extra step of 10 min at 37 °C was added at the beginning of the reverse transcription protocol. Post GEM-RT cleanup and cDNA amplification (15 cycles) was performed as per the manufacturer's instructions and 10 μL of purified cDNA was used for sequencing library construction. The final library was quality checked using the High Sensitivity DNA Kit and a Bioanalyzer (Agilent) and sequencing was performed using a NovaSeq 6000 (Illumina).

For experiments that combined FACS with scRNA-Seq, cells were aged in MADs, purified as above and stained with Dylight (viability) and Wheat Germ Agglutinin (WGA; bud scars) for 10 min while kept in TAF buffer on ice. For both the Srp40-mNeon and MMP sorts, Dylight-680 and WGA-405 (Thermo Fisher) were used. Only Dylight-negative and WGA-high cells were included. For binning, cells were sorted into "low" and "high" subpopulations as defined by the top or bottom 25% of Srp40 fluorescence or the MMP ratio (24), respectively. Cells were in the presence of 1 U/μL Protector RNase Inhibitor from harvest until chip loading and kept on ice whenever possible. Loading into the Chromium chip and processing for scRNA-Seq was done as above.

scRNA-Seq reads were aligned to the genome using kallisto bustools [kb count with default arguments; kb_python v0.27.1; kallisto: v0.48.0; bustools: v0.41.0; (42, 43)]. The custom reference genome was generated by selecting the largest annotated feature for each gene annotated in the Saccharomyces Genome Database. Subsequent analysis was done using scanpy (v1.11.0). First, each sample was filtered to an appropriate number of cells by identifying the "knee point" where the number of unique reads per barcode dramatically dropped. Genes expressed in fewer than 10 cells were removed, and cells with fewer than 1,000 unique detected genes were also removed to filter out low-quality or empty

droplets. Library size differences between the remaining cells were normalized by scaling the counts in each cell to a total of 1,000,000 reads. Finally, the data were log transformed as $X = \log(X + 1)$.

RLS Measurements. RLS was measured in YLMs as described in refs. 21 and 27. Cells were grown for 24 h at OD < 0.05 before loading into microfluidics devices containing polydimethylsiloxane catcher structures designed to retain aging mother cells, while continuously washing away daughter cells. These devices had 24 channels in parallel with each channel containing ~1000 "DetecDiv"-style catchers (44). Brightfield images were collected every 15 min for 96 h. Time-lapse images were analyzed by an automated computer vision pipeline, counting the number of divisions and the terminal outcome of a cell's lifespan [death vs. censoring/washout; (21)]. Median lifespan was determined by using the Kaplan–Meier estimate of the survival function. MoD was determined with a separate machine learning model (as described in ref. 27).

Fluorescent Time-Lapse Microscopy. For fluorescent time-lapse imaging, the YLM systems were modified with custom epifluorescence illumination. Excitation light was supplied by a Thorlabs high-power LED and filtered using a band-pass filter appropriate for each fluorophore. Multipass dichroic beamsplitters, and multipass emissions filters were used to minimize moving components. To minimize phototoxicity and photobleaching, images were acquired at 2 h intervals.

Flow Cytometry on IRFP in Media Containing 5-Aminolevulinic Acid (5-ALA). *Hem1*Δ cells were grown for 24 h at OD < 0.05 in SC medium containing 10 μg/mL of the heme precursor 5-ALA. Cells were diluted into media containing 0, 10, 25, 50, or 300 μg/mL 5-ALA and grown for 6 h, stained with 1 μM SYTOX Blue (Thermo Fisher) and then analyzed on a LSRFortessa X-20 Cell Analyzer (Becton Dickinson) using the appropriate lasers and filters. Live cells were gated using the Sytox Blue signal and at least 10,000 cells per condition were analyzed. A WT strain without integrated iRFP was used as control.

Bulk RNA-Seq and Analysis. Exponentially growing (young) or aged (24 h) cells were harvested and washed in RNA-Later (Sigma-Aldrich) and frozen at −80 °C. Bulk RNA-seq was performed by Admera Health. Total RNA was extracted and purified using the RNeasy Plant Mini Kit for RNA Extraction (Qiagen). RNA was quality-controlled and quantified using a TapeStation (Agilent) and only high quality samples (RNA integrity number >6) were used. The NEB Ultra II Directional RNA Library Prep Kit (New England BioLabs Inc.) was used to generate cDNA and sequencing libraries. Libraries were indexed using Admera's in-house index primers and cleaned with AFTMag NGS DNA Clean Beads (Abclonal). The indexed libraries were pooled and sequenced on the Illumina NovaSeq X plus platform with a read length of 2 × 150 bp. Raw sequencing reads were demultiplexed with bcl2fastq. Differential gene expression was calculated using DESeq2 (45).

Whole-Genome Sequencing for rDNA CN Estimation. Genomic DNA was extracted as described before (27). Briefly, cells were grown overnight in Yeast Extract Peptone Dextrose medium, washed 1× with sterile water and genomic DNA was extracted using the YeaStar Genomic DNA kit (Zymo Research). Library preparation and sequencing were performed by Admera Health. In brief, gDNA samples were subjected to fragmentation and adaptor ligation using the Kapa Hyper Prep (Roche), following the manufacturer's standard protocol. Libraries were pooled and sequenced on the Illumina NovaSeq X plus platform with a read length of 2 × 150 bp. The sequencing was performed to yield a minimum of 60 million paired-end reads. Raw sequencing data were demultiplexed with bcl2fastq. rDNA CN estimation was done as previously described (27). Reads were aligned to the *S. cerevisiae* genome (sacCer3, Release 64) using bowtie2 version 2.3.5.1 with default parameters. CN was estimated by calculating the average read depth at three locations on Chromosome 12: 2 single copy loci (Chr12:760000. 790000 and Chr12:160000. 190000), and one in the rDNA locus (Chr12:451575. 468931). CN was estimated to be median(rDNA locus depth)/mean[median(Chr12-L1 depth), median(Chr12-L2 depth)].

Respiratory Capacity. Respiratory capacity was assessed using either exponentially growing, young cells or cells aged in MADs that had been purified on magnets as described above. Cells were diluted and plated at an approximate density of ~150 colonies per plate. Plates were incubated at 30 °C for 48 h and then replica plated onto Yeast Extract Peptone Glycerol Ethanol plates. Colonies were counted on both YPD and YPEG plates to quantify the fraction of petite cells.

GSEA. GSEA was performed with the GSEApy Python package v1.1.6 (46). Briefly, genes were preranked using their differential gene expression (calculated as t-score; Dataset S1). Gene sets were obtained from the Saccharomyces Genome Database with the added gene ontology term "ESR induced" for genes upregulated during ESR induction (see Dataset S2 for complete list of gene ontology terms).

Hazard Analysis and Modeling. Linear Mixed-Effects Models were used to analyze the dynamics of fluorescent reporter signals over the cellular lifespan. Age was modeled as a fraction of the total lifespan in divisions. This approach modeled the fluorescent trajectory as a quadratic function of cell age (age + age**2). The model tested for an interaction between the quadratic age terms and genotype, allowing the trajectory shape to differ for each genotype. Random effects for each individual cell's intercept, linear, and quadratic age terms (1 + age + age**2|cell) were included to account for cell-to-cell variability. The models were fit using the statsmodels Python package.

Cox Proportional Hazard models were used to determine how different genotypes influenced the replicative age at which key cellular events occurred in each cell. Events were defined as follows. For MMP and heme decline, the event was called when four consecutive fluorescent measurements (preCOX4-mNeon and iRFP, respectively) were below 0.8 fold the initial level (mean of the first five measurements). For ERC accumulation and ESR induction, the event was called when four consecutive fluorescent measurements (Srp40-mCherry and Hsp12-mCherry, respectively) were above 1.2 fold the initial level. Age was modeled as a fraction of the total lifespan in divisions. This analysis identified whether a specific genotype made an event more or less likely to happen at any given age compared to WT. These models were fit using the lifelines Python package.

Data, Materials, and Software Availability. Bulk RNA-Seq raw data are accessible at Gene Expression Omnibus [GSE318874; (47)]. ScRNA-Seq raw data are accessible at Gene Expression Omnibus [GSE318875; (48)]. All other data are included in the manuscript and/or supporting information.

ACKNOWLEDGMENTS. We would like to thank: members of the Calico Genomics groups for DNA and RNA sequencing, in particular Evangelia Malahias for help with testing the scRNA-Seq method. Anurag Sethi and Graham Ruby for helpful discussions about statistical modeling. Reinhard Dechant and Kiyan Shabestary for critical reading of the manuscript.

Author affiliations: [a]Calico Life Sciences LLC, South San Francisco, CA 94080

Author contributions: M.H., R.G.K.-L., N.H.T., and D.E.G. designed research; M.H., R.G.K.-L., and N.H.T. performed research; M.H., R.G.K.-L., and N.H.T. analyzed data; and M.H., R.G.K.-L., N.H.T., and D.E.G. wrote the paper.

Reviewers: T.N., Goteborgs universitet Sahlgrenska Akademin; and J.S.S., University of Virginia.

Competing interest statement: All are employed by Calico Life Sciences LLC. The work presented here is not of commercial value to Calico, but rather a contribution to advancing the study of yeast aging.

1. V. Castelli *et al.*, Neuronal cells rearrangement during aging and neurodegenerative disease: Metabolism, oxidative stress and organelles dynamic. *Front. Mol. Neurosci.* **12**, 132 (2019).
2. A. Vakka, J. S. Warren, K. Drosatos, Cardiovascular aging: From cellular and molecular changes to therapeutic interventions. *J. Cardiovasc. Aging* **3**, 23 (2023).
3. M. V. Wrona, R. Ghosh, K. Coll, C. Chun, M. J. Yousefzadeh, The 3 i's of immunity and aging: Immunosenescence, inflammaging, and immune resilience. *Front. Aging* **5**, 1490302 (2024).
4. P. Goyani, R. Christodoulou, E. Vassiliou, Immunosenescence: Aging and immune system decline. *Vaccines (Basel)* **12**, 1314 (2024).
5. C. Gizowski *et al.*, Heterochronic myeloid cell replacement reveals the local brain environment as key driver of microglia aging. bioRxiv [Preprint] (2025). https://doi.org/10.1101/2025.09.02.673859 (Accessed 1 January 2026).
6. J. R. Johnston, Reproductive capacity and mode of death of yeast cells. *Antonie Van Leeuwenhoek* **32**, 94–98 (1966).
7. A. Denoth Lippuner, T. Julou, Y. Barral, Budding yeast as a model organism to study the effects of age. *FEMS Microbiol. Rev.* **38**, 300–325 (2014).
8. M. Jin *et al.*, Divergent aging of isogenic yeast cells revealed through single-cell phenotypic dynamics. *Cell Syst.* **8**, 242.e3–253.e3 (2019).

9. Y. Li *et al.*, A programmable fate decision landscape underlies single-cell aging in yeast. *Science* **369**, 325–329 (2020).
10. D. A. Sinclair, L. Guarente, Extrachromosomal rDNA circles–A cause of aging in yeast. *Cell* **91**, 1033–1042 (1997).
11. D. G. Hendrickson *et al.*, A new experimental platform facilitates assessment of the transcriptional and chromatin landscapes of aging yeast. *Elife* **7**, e39911 (2018).
12. A. P. Gasch *et al.*, Genomic expression programs in the response of yeast cells to environmental changes. *Mol. Biol. Cell* **11**, 4241–4257 (2000).
13. S. Leupold *et al.*, Saccharomyces cerevisiae goes through distinct metabolic phases during its replicative lifespan. *Elife* **8**, e41046 (2019).
14. M. Leutert *et al.*, Multidimensional proteomics identifies molecular trajectories of cellular aging and rejuvenation. bioRxiv [Preprint] (2023). https://doi.org/10.1101/2023.03.09.531951 (Accessed 1 January 2026).
15. J. Wang *et al.*, Single-cell RNA-seq reveals early heterogeneity during aging in yeast. *Aging Cell* **21**, e13712 (2022).
16. C. A. Jackson, D. M. Castro, G. A. Saldi, R. Bonneau, D. Gresham, Gene regulatory network reconstruction using single-cell RNA sequencing of barcoded genotypes in diverse environments. *Elife* **9**, e51254 (2020).
17. M. Nadal-Ribelles *et al.*, A single-cell resolved genotype-phenotype map using genome-wide genetic and environmental perturbations. *Nat. Commun.* **16**, 2645 (2025).
18. M. J. Brauer *et al.*, Coordination of growth rate, cell cycle, stress response, and metabolic activity in yeast. *Mol. Biol. Cell* **19**, 352–367 (2008).
19. B. M. Tsoi *et al.*, Essential role of one-carbon metabolism and gcn4p and bas1p transcriptional regulators during adaptation to anaerobic growth of *Saccharomyces cerevisiae*. *J. Biol. Chem.* **284**, 11205–11215 (2009).
20. T. Zhang, P. Bu, J. Zeng, A. Vancura, Increased heme synthesis in yeast induces a metabolic switch from fermentation to respiration even under conditions of glucose repression. *J. Biol. Chem.* **292**, 16942–16954 (2017).
21. N. H. Thayer *et al.*, The yeast lifespan machine: A microfluidic platform for automated replicative lifespan measurements. bioRxiv [Preprint] (2022). https://doi.org/10.1101/2022.02.14.480146 (Accessed 1 January 2026).
22. M. T. Martínez-Pastor *et al.*, The Saccharomyces cerevisiae zinc finger proteins msn2p and msn4p are required for transcriptional induction through the stress response element (STRE). *EMBO J.* **15**, 2227–2235 (1996).
23. A. L. Hughes, D. E. Gottschling, An early age increase in vacuolar pH limits mitochondrial function and lifespan in yeast. *Nature* **492**, 261–265 (2012).
24. A. J. Waite *et al.*, Potassium ion homeostasis modulates mitochondrial function. *J. Cell Biol.* **225**, e202505110 (2026).
25. T. Suhm *et al.*, A novel system to monitor mitochondrial translation in yeast. *Microb. Cell* **5**, 158–164 (2018).
26. O. Medvedik, D. W. Lamming, K. D. Kim, D. A. Sinclair, MSN2 and MSN4 link calorie restriction and TOR to sirtuin-mediated lifespan extension in *Saccharomyces cerevisiae*. *PLoS Biol.* **5**, e261 (2007).
27. M. Hotz *et al.*, rDNA array length is a major determinant of replicative lifespan in budding yeast. *Proc. Natl. Acad. Sci. U.S.A.* **119**, e2119593119 (2022).
28. G. S. Filonov *et al.*, Bright and stable near-infrared fluorescent protein for in vivo imaging. *Nat. Biotechnol.* **29**, 757–761 (2011).
29. J. Rine, I. Herskowitz, Four genes responsible for a position effect on expression from HML and HMR in *Saccharomyces cerevisiae*. *Genetics* **116**, 9–22 (1987).
30. O. M. Aparicio, B. L. Billington, D. E. Gottschling, Modifiers of position effect are shared between telomeric and silent mating-type loci in Saccharomyces cerevisiae. *Cell* **66**, 1279–1287 (1991).
31. M. Kaeberlein, M. McVey, L. Guarente, The SIR2/3/4 complex and SIR2 alone promote longevity in Saccharomyces cerevisiae by two different mechanisms. *Genes Dev.* **13**, 2570–2580 (1999).
32. S. Imai, C. M. Armstrong, M. Kaeberlein, L. Guarente, Transcriptional silencing and longevity protein Sir2 is an NAD-dependent histone deacetylase. *Nature* **403**, 795–800 (2000).
33. A. Caballero *et al.*, Absence of mitochondrial translation control proteins extends life span by activating sirtuin-dependent silencing. *Mol. Cell* **42**, 390–400 (2011).
34. R. Higuchi *et al.*, Actin dynamics affect mitochondrial quality control and aging in budding yeast. *Curr. Biol.* **23**, 2417–2422 (2013).
35. P. A. Defossez *et al.*, Elimination of replication block protein fob1 extends the life span of yeast mother cells. *Mol. Cell* **3**, 447–455 (1999).
36. J. R. Veatch, M. A. McMurray, Z. W. Nelson, D. E. Gottschling, Mitochondrial dysfunction leads to nuclear genome instability via an iron-sulfur cluster defect. *Cell* **137**, 1247–1258 (2009).
37. E. J. N. Yang, P. C. Liao, L. Pon, Mitochondrial protein and organelle quality control–lessons from budding yeast. *IUBMB Life* **76**, 72–87 (2024).
38. M. N. Devare *et al.*, TORC1 signaling regulates cytoplasmic ph through sir2 in yeast. *Aging Cell* **19**, e13151 (2020).
39. C. Janke *et al.*, A versatile toolbox for PCR-based tagging of yeast genes: New fluorescent proteins, more markers and promoter substitution cassettes. *Yeast* **21**, 947–962 (2004).
40. M. A. Sheff, K. S. Thorn, Optimized cassettes for fluorescent protein tagging in *Saccharomyces cerevisiae*. *Yeast* **21**, 661–670 (2004).
41. W. P. Voth, J. D. Richards, J. M. Shaw, D. J. Stillman, Yeast vectors for integration at the HO locus. *Nucleic Acids Res.* **29**, E59–E159 (2001).
42. N. L. Bray, H. Pimentel, P. Melsted, L. Pachter, Near-optimal probabilistic RNA-seq quantification. *Nat. Biotechnol.* **34**, 525–527 (2016).
43. P. Melsted *et al.*, Modular, efficient and constant-memory single-cell RNA-seq preprocessing. *Nat. Biotechnol.* **39**, 813–818 (2021).
44. T. Aspert, D. Hentsch, G. Charvin, DetecDiv, a generalist deep-learning platform for automated cell division tracking and survival analysis. *Elife* **11**, e79519 (2022).
45. M. I. Love, W. Huber, S. Anders, Moderated estimation of fold change and dispersion for RNA-seq data with DESeq2. *Genome Biol.* **15**, 550 (2014).
46. Z. Fang, X. Liu, G. Peltz, GSEApy: A comprehensive package for performing gene set enrichment analysis in python. *Bioinformatics* **39**, btac757 (2023).
47. M. Hotz *et al.*, Single-cell analyses identify independent aging processes that compete to determine cellular fate in budding yeast–Bulk RNA-Seq. Gene Expression Omnibus. https://www.ncbi.nlm.nih.gov/geo/query/acc.cgi?acc=GSE318874. Deposited 9 February 2026.
48. M. Hotz *et al.*, Single-cell analyses identify independent aging processes that compete to determine cellular fate in budding yeast–scRNA-seq. Gene Expression Omnibus. https://www.ncbi.nlm.nih.gov/geo/query/acc.cgi?acc=GSE318875. Deposited 9 February 2026.